A real liquid volume-of-fluid framework with evaporation dynamics

Lorenzo Angelilli, Venkat Raman
University of Michigan
Ann Arbor, Michigan, 48109, US

Abstract

This study presents an evaporation model integrated into a Volume of Fluid (VOF) solver that incorporates a tabulated equation of state (EOS) for the liquid phase. The model builds upon the canonical interface evaporation model and is implemented in an adaptive mesh refinement (AMR) solver developed using AMReX. Key features of the model include explicit consideration of interfacial mass transfer, strict enforcement of energy conservation, and thermodynamic consistency to capture the intricate dynamics at the liquid-gas interface. Preliminary results suggest that this integrated model successfully predicts evaporation rates and temperature distributions in simple flow scenarios.

1 Introduction

Shock-droplet interactions are vital in applications such as fuel injection for rotating detonation engines [1] and scramjets [2, 3]. When a shock wave impinges on a liquid droplet, rapid deformation, breakup, and phase transitions occur [4], significantly affecting the performance and stability of detonation-based combustors. High detonation wave speeds allow little time for droplet evaporation and mixing, making accurate modeling of these processes critical [5].

Several evaporation models have been developed to enhance the predictive capability of VOF-based simulations [6]. Early approaches relied on equilibrium-based formulations, assuming instantaneous phase change at the interface based on local thermodynamic conditions [7]. More advanced models incorporate non-equilibrium effects, considering kinetic limitations and transport resistances that affect interfacial mass flux [8]. The work of Hardt and Wondra [9] introduced an evaporation model based on the Hertz-Knudsen equation, accounting for the effects of interfacial temperature and pressure gradients. Additionally, the sharp-Interface [10] and diffuse-Interface models [8] have been explored to improve numerical accuracy in phase-change simulations. However, most existing approaches rely on idealized equations of state (EOS), which may limit their accuracy when dealing with real fluids under non-ideal thermodynamic conditions [11].

In this study, we present an evaporation model integrated with a VOF solver that incorporates a real equation of state (EOS) for the liquid phase. The use of a real EOS enables a more accurate representation of thermophysical properties, particularly in cases involving high pressures and non-ideal vapor-liquid equilibrium. Our approach explicitly accounts for interfacial mass transfer, energy conservation, and thermodynamic consistency within the VOF framework. The model, presented in the Sec. 2, is implemented in an AMREX-based solver [12] and the preliminary results are presented in the manuscript.

Correspondence to: langelil@umich.edu

2 Numerical Methods

The one-dimensional conservation laws for multiphase flow read as:

$$\frac{\partial \alpha_l}{\partial t} + \mathbf{u} \cdot \nabla \alpha = \beta(P_l - P_g), \tag{1}$$

$$\frac{\partial \alpha_l \rho_l}{\partial t} + \nabla \cdot (\alpha_l \rho_l \mathbf{u}) = 0, \tag{2}$$

$$\frac{\partial \alpha_g \rho_g}{\partial t} + \nabla \cdot (\alpha_g \rho_g \mathbf{u}) = 0, \tag{3}$$

$$\frac{\partial \alpha_g \rho_g Y_\alpha}{\partial t} + \nabla \cdot (\alpha_g \rho_g Y_\alpha \mathbf{u}) = \nabla \cdot (\alpha_g \rho_g D_\alpha \nabla Y_\alpha) + \dot{\omega}_\alpha \qquad \forall \alpha, \tag{4}$$

$$\frac{\partial \rho \mathbf{u}}{\partial t} + \nabla \cdot (\rho \mathbf{u} \otimes \mathbf{u} + P\mathbf{I}) = \nabla \cdot \boldsymbol{\tau}, \tag{5}$$

$$\frac{\partial \alpha_l \rho_l e_l}{\partial t} + \nabla \cdot (\alpha_l \rho_l e_l \mathbf{u}) + \alpha_l P_l \nabla \cdot \mathbf{u} = \nabla \cdot (\alpha_l \boldsymbol{\tau} \cdot \mathbf{u}) + \nabla \cdot (\lambda_l \nabla T_l) + \beta P_I (P_l - P_g), \tag{6}$$

$$\frac{\partial \alpha_g \rho_g e_g}{\partial t} + \nabla \cdot (\alpha_g \rho_g e_g \mathbf{u}) + \alpha_g P_g \nabla \cdot \mathbf{u} = \nabla \cdot (\alpha_g \boldsymbol{\tau} \cdot \mathbf{u}) + \nabla \cdot (\lambda_g \nabla T_g) - \beta P_I (P_l - P_g), \tag{7}$$

where Eq. 1 is the non-conservative transport equation for the liquid volume fraction, Eqs. 2 and 3 are the conservative transport equation for the liquid and gas mass respectively, Eq. 4 is the advection-diffusion equation for the gaseous species mass fractions, Eq. 5 is the total momentum conservation law, Eqs. 6 and 7 are the nonconservative transport equations for the liquid and gas internal energy components. Note that by manipulating Eqs. 6, 7 and 5 it is possible to obtain the conservation law of the total energy, but in this work it is not resolved. In the aforementioned equations, α_l and α_g are the liquid and gas volume fractions, $\mathbf{u}$ the velocity vector, ρ_l and ρ_g the liquid and gas densities, while $\rho = \alpha_l \rho_l + \alpha_g \rho_g$ is the mixture density, Y_α, D_α, $\dot{\omega}_\alpha$ are the mass fraction, diffusivity, and chemical source term of the species α, P_l and P_g the liquid and gas pressure and $P = \alpha_l P_l + \alpha_g P_g$ the mixture pressure, T_l and T_g are the liquid and gas temperature, and λ_l and λ_g the liquid and gas thermal conductivities.

The gaseous internal energy is given by $e_g = \sum_\alpha \left(\Delta h^0_{f,\alpha} Y_\alpha + \int_{T_0}^{T_g} C_{p,\alpha}(T) dT \right) - \frac{P_g}{\rho_g}$, where $\Delta h^0_{f,\alpha}$ is the formation enthalpy of the species α, $C_{p,\alpha}$ is its constant pressure heat capacity. The liquid internal energy is given by $e_l = \int_{T_0}^{T_l} C_l(T) dT$, where C_l is the liquid heat capacity. In the viscous stress tensor $\boldsymbol{\tau}$ the viscosity of the mixture is defined as $\mu = \alpha_l \mu_l + \alpha_g \mu_g$, where μ_l and μ_g the liquid and gas viscosity.

In this solver, the assumption of constant liquid properties is relaxed by interpolating all liquid properties (μ_l, C_l, and λ_l) from the NIST database using NSDRS functions. The gas properties are obtained from Cantera and NASA polynomials. The gas pressure is determined by the ideal gas law, $P_g = \rho_g R_g T_g$, while the liquid equation of state is numerically derived by performing a bicubic spline interpolation of the P–v–T diagram from the NIST database.

The set of equations is solved in two steps. As shown in previous works [8], the acoustic interaction between the two phases is represented by the very stiff terms ($\beta(P_l - P_g)$ and $\pm\beta P_I(P_l - P_g)$) in Eqs. 6 and 7. Under the assumption that $\beta \to \infty$, each computational cell is first solved by setting $\beta = 0$, followed by a stiff analytical relaxation step.

The hyperbolic system is solved using the Harten-Lax-van Leer Contact (HLLC) approximate Riemann solver and advanced in time with an explicit second-order Runge–Kutta scheme, as described in [12]. To accommodate the real equation of state, the expanded liquid state resulting from the solution of the

approximate Riemann problem is evaluated by applying the isentropic relation from Tait's equation of state:

$$P = P_0 + K_s(T_0)\left[\left(\frac{\rho}{\rho_0}\right)^n - 1\right] \tag{8}$$

where K_s is the adiabatic bulk modulus of the liquid and n is the Tait index (commonly $n = 7$).

The stiff relaxation step is performed by assuming only mechanical equilibrium ($P_l = P_g$) in a liquid–gas mixture cell. In contrast to the common assumption of thermal equilibrium, this work employs distinct temperatures for the liquid and gas within a single computational cell. Physically, thermal equilibrium is restricted to the interface, whose thickness is on the order of a fraction of a nanometer, a length scale that remains computationally prohibitive. Consequently, there is no justification for the assumption that the liquid and gas have the same temperature.

Because the liquid and gas masses, as well as the total internal energy, are conserved, the following system can be written:

$$\begin{cases} \alpha_l + \alpha_g = 1 \\ \rho_l \alpha_l = \rho_l^0 \alpha_l^0 = C_l \\ \rho_g \alpha_g = \rho_g^0 \alpha_g^0 = C_g \\ \rho_l e_l \alpha_l + \rho_g e_g \alpha_g = \rho_l^0 e_l^0 \alpha_l^0 + \rho_g^0 e_g^0 \alpha_g^0 = C_e \end{cases} \tag{9}$$

where the superscript ^{0} refers to quantities obtained from the advection step. In this work, we assume that the phasic internal energy is not affected by the acoustic interaction between the two phases. Consequently, the last constraint in the system is always automatically satisfied.

Since the liquid density does not vary significantly, the system can be numerically solved by iteratively computing the pressure as

$$P^{n+1} = \frac{R_g T_g C_g}{1 - \frac{C_l}{\rho_l(P^n, T_l)}} \tag{10}$$

and then determining the liquid and gas volume fractions. Similarly to the temperature, for the evaporation model the liquid-vapor equilibrium assumption holds exclusively at the interface, not in the entire computational cell. This assumption generates nonphysical results if the α_l or α_g are small, or overestimates the amount of evaporated mass. Indeed this assumption is only volume-dependent and time-independent.

For these reasons, this work presents a new evaporation model that estimates the evaporated mass, liquid and gas temperatures, and the pressure within a single cell. Assuming the interface is contained within a single cell, the mass transfer rate can be expressed based on the diffusion theory of Law [13]:

$$\dot{m}_{evap,\alpha} = -\frac{\rho_g D_\alpha}{\ell} \log(1 + B_M) \qquad B_M = \frac{Y_s - Y_\alpha}{1 - Y_s} \qquad \ell = \frac{\alpha_g V_c}{A_i} \tag{11}$$

where V_c is the cell volume and A_i is the interfacial area. The surface mass fraction Y_s of the evaporating species is determined by the thermal and liquid–vapor equilibrium:

$$Y_s = Y_{sat}(T_s) = \frac{Y_g + B_H}{1 + B_H} \qquad B_H = \frac{C_{P,g}(T_g - T_s)}{L_v(T_s)} \tag{12}$$

where Y_{sat} is the saturation mass fraction, T_s is the surface temperature, and L_v is the latent heat of vaporization. The saturation pressure, as a function of the gas temperature, is obtained by interpolating the NIST data. Equation 11 is numerically integrated to estimate the evaporated mass and update the

gas-phase composition. To determine the liquid and gas temperatures within the computational cell, the one-dimensional transient heat equation is solved:

$$\frac{\partial T}{\partial t} = k_{l,g}\frac{\partial^2 T}{\partial x^2}, \quad 0 < x < \ell_{l,g},\, t > 0 \tag{13}$$

with boundary conditions $T(0,t) = T_s$ and $T(\ell_{l,g},t) = T_{l,g}$, and initial condition $T(x,0) = T_{l,g}$. The heat diffusivity is given by $k_{l,g} = \lambda_{l,g}/(\rho_{l,g}C_{l,g})$. For simplicity, constant heat capacity and thermal conductivity are assumed, which allows for an analytical solution:

$$T_{l,g}(x,t) = \frac{T_s - T_{l,g}}{\ell_{l,g}}x + T_{l,g} + \sum_{n=1}^{\infty}\frac{2(T_s - T_{l,g})}{n\pi}(-1)^n \sin\left(\frac{n\pi x}{\ell_{l,g}}\right) e^{-k_{l,g}\left(\frac{n\pi}{\ell_{l,g}}\right)^2 t} \tag{14}$$

The liquid (or gas) temperature in the cell is then found by taking the integral average

$$\overline{T}_{l,g}(t) = \frac{1}{\ell_{l,g}}\int_0^{\ell_{l,g}} T_{l,g}(x,t)dx = \frac{T_s + T_{l,g}}{2} - 4(T_s - T_{l,g})\sum_{n=1,3,5,\ldots}^{\infty}\frac{1}{(n\pi)^2}e^{-k_{l,g}\left(\frac{n\pi}{\ell_{l,g}}\right)^2 t} \tag{15}$$

where $\ell_{l,g} = (\alpha_{l,g}V_c)/A_i$. In a manner analogous to the pressure relaxation step (Eq. 9), P, α_g, and α_l are recomputed to ensure conservation of total (liquid + gas) mass and energy in the computational cell, by numerically solving the relevant mass and energy conservation equations.

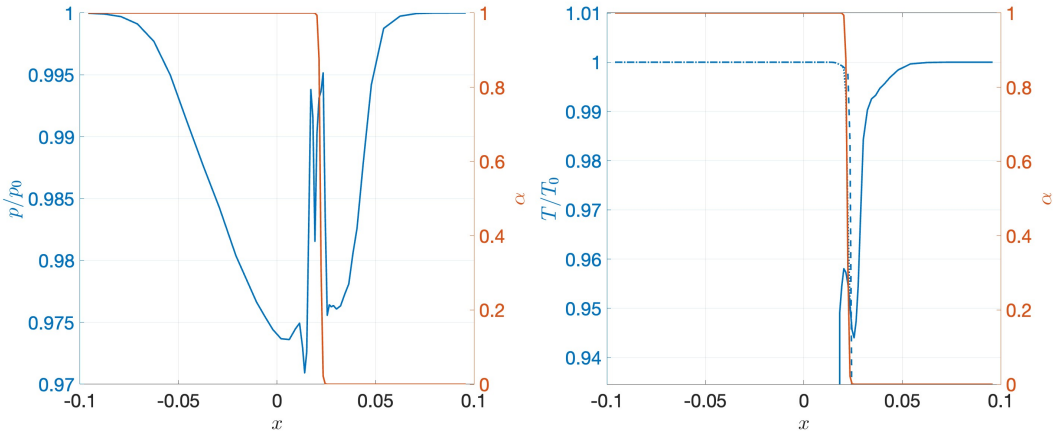

Figure 1: Pressure and Temperature profiles after 100 time steps. In temperature panel: continuous line is gas temperature; dashed line is the liquid temperature. Orange line is the volume fraction in both panels.

3 Results

To leverage the Adaptive Mesh Refinement (AMR) capabilities for resolving the interface, the proposed model has been integrated into an in-house AMReX-based compressible flow solver [12]. The preliminary test case presented here examines one-dimensional evaporation of liquid water in air. Initially, both phases are at 300 K and atmospheric pressure, flowing from left to right at 400 m/s. The computational domain extends 2 cm and is discretized by 24 cells at the coarsest level. The simulation employs five AMR levels, achieving a finest grid resolution of 26 μm at the interface, thus allowing for accurate capture of phase-change processes and interfacial dynamics.

Figure 1 shows the pressure and temperature profiles after 100 time steps. Introducing evaporated mass from the liquid to the gas phase induces pressure oscillations within the computational cells, as mass, momentum, and energy are conserved. Although these oscillations are sensitive to the time-step size and can introduce numerical stiffness, their impact remains limited: with a Courant-Friedrichs-Lewy (CFL) number of 0.3, the maximum pressure fluctuation is under 3%, resulting in negligible effects on momentum and evaporation dynamics. The tabulated Equation of State (EoS) accurately represents the liquid's incompressibility under the given conditions, ensuring that these moderate pressure changes do not significantly alter liquid density or temperature. The temperature decreases sharply near the interface, reaching a minimum of 283.5 K in both the liquid and gas phases. This value compares favorably with the 281.3 K predicted by the liquid–vapor equilibrium correlation (Eq. 12). Owing to different thermal diffusivities in the liquid and gas phases, their respective temperature gradients vary before both profiles asymptotically recover to the initial 300 K.

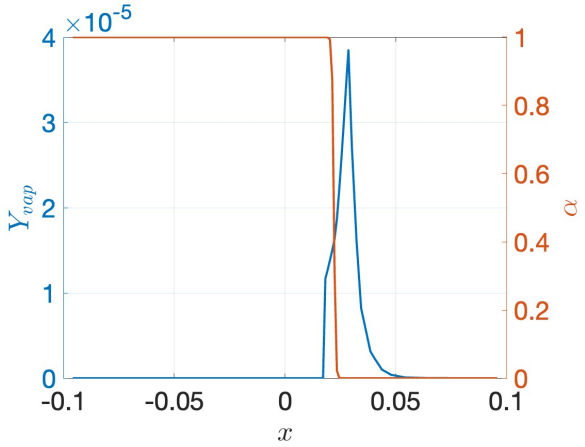

Figure 2: Vapor mass fraction profiles after 100 time steps.

Figure 2 shows the vapor species mass fraction profiles. Because the saturation composition is expected exclusively at the interface, it takes time for any computational cell to approach that saturation level. Even after 100 time steps, the maximum mass fraction is 3.9×10^{-5}, which is significantly lower than the actual saturation composition ($Y_{sat} = 0.0083$). Traditional approaches directly assign Y_{sat} to each computational cell, resulting in local pressures considerably lower than the ambient pressure and leading to strong pressure oscillations. In contrast, this model derives the released vapor mass from well-validated mass transfer rates, ensuring that pressure, temperature, and vapor mass fractions remain consistent with the surrounding environment.

4 Conclusion

This manuscript presented a new evaporation model integrated into a solver that employs a tabulated equation of state. Preliminary simulations of water–air evaporation demonstrate the model's ability to capture the expected temperature drop and time-dependent evaporation behavior. Notably, the approach mitigates pressure oscillations arising from the mass transfer of vapor into the gas phase. These promising outcomes pave the way for further development of a fully multi-dimensional solver, facilitating the study of more complex flow configurations and enhancing the predictive capability for a broad range of evaporation-driven applications.

References

[1] Hao Liu, Feilong Song, Di Jin, Shida Xu, and Xingkui Yang. Experimental investigation on spray and detonation initiation characteristics of premixed/non-premixed rde. *Fuel*, 331:125949, 2023.

[2] Zhaoxin Ren, Bing Wang, Gaoming Xiang, Dan Zhao, and Longxi Zheng. Supersonic spray combustion subject to scramjets: Progress and challenges. *Progress in Aerospace Sciences*, 105:40–59, 2019.

[3] Shivank Sharma, Jagmohan Singh, Lorenzo Angelilli, and Venkat Raman. Interaction of chemical reactions and turbulence in a jet in supersonic crossflow. *Proceedings of the Combustion Institute*, 40(1-4):105295, 2024.

[4] Shubham Sharma, Awanish Pratap Singh, S Srinivas Rao, Aloke Kumar, and Saptarshi Basu. Shock induced aerobreakup of a droplet. *Journal of Fluid Mechanics*, 929:A27, 2021.

[5] Venkat Raman, Supraj Prakash, and Mirko Gamba. Nonidealities in rotating detonation engines. *Annual Review of Fluid Mechanics*, 55(1):639–674, 2023.

[6] KMT Kleefsman, G Fekken, AEP Veldman, B Iwanowski, and B Buchner. A volume-of-fluid based simulation method for wave impact problems. *Journal of computational physics*, 206(1):363–393, 2005.

[7] Richard Saurel and Olivier Lemetayer. A multiphase model for compressible flows with interfaces, shocks, detonation waves and cavitation. *Journal of fluid mechanics*, 431:239–271, 2001.

[8] Richard Saurel, Pierre Boivin, and Olivier Le Métayer. A general formulation for cavitating, boiling and evaporating flows. *Computers & Fluids*, 128:53–64, 2016.

[9] Steffen Hardt and Frank Wondra. Evaporation model for interfacial flows based on a continuum-field representation of the source terms. *Journal of Computational Physics*, 227(11):5871–5895, 2008.

[10] Johan Roenby, Henrik Bredmose, and Hrvoje Jasak. A computational method for sharp interface advection. *Royal Society open science*, 3(11):160405, 2016.

[11] Olivier Le Métayer and Richard Saurel. The noble-abel stiffened-gas equation of state. *Physics of Fluids*, 28(4), 2016.

[12] Shivank Sharma, Ral Bielawski, Oliver Gibson, Shuzhi Zhang, Vansh Sharma, Andreas H Rauch, Jagmohan Singh, Sebastian Abisleiman, Michael Ullman, Shivam Barwey, et al. An amrex-based compressible reacting flow solver for high-speed reacting flows relevant to hypersonic propulsion. *arXiv preprint arXiv:2412.00900*, 2024.

[13] Chung K Law. *Combustion physics*. Cambridge university press, 2010.